Ohmic resistance of nickel infiltrated chromium oxide scales in solid oxide fuel cell metallic interconnects

Markus Linder[a,b,*], Thomas Hocker[a], Lorenz Holzer[a], Omar Pecho[a], K. Andreas Friedrich[b], Tobias Morawietz[c], Renate Hiesgen[c], Roman Kontic[d], Boris Iwanschitz[e], Andreas Mai[e], J. Andreas Schuler[e]

[a] *ZHAW Zurich University of Appl. Sciences, Institute of Computational Physics, Technikumstrasse 9, CH-8401 Winterthur, Switzerland*
[b] *Deutsches Zentrum für Luft- und Raumfahrt, Institute of Engineering Thermodynamics, Pfaffenwaldring 38-40, D-70569 Stuttgart, Germany*
[c] *University of Applied Sciences Esslingen, Department of Basic Science, D-73728 Esslingen, Germany*
[d] *ZHAW Zurich University of Appl. Sciences, Institute of Materials and Process Engineering, Technikumstrasse 9, CH-8401 Winterthur, Switzerland*
[e] *Hexis AG, Zum Park 5, CH-8404 Winterthur, Switzerland*

Abstract

Oxide scale formation on metallic interconnects contributes to the overall degradation of solid oxide fuel cell (SOFC) stacks. On the anode side, thermally grown oxide scale might contain additional nickel, nickel oxide, or nickel chromium spinel phases – depending on the applied operation conditions. Ni originates from Ni-meshes, often applied as current collector, from Ni-containing anodes or from Ni-containing coatings. Ni particles released during thermo redox cycles from adjacent Ni-containing components might be interspersed into the oxide scale. This study aims at investigating the influence of Ni on the electrical conductivity of oxide scales. For this purpose pellets of Cr_2O_3 were mixed with different amounts of Ni and then investigated in-situ under both reducing and oxidizing gas atmospheres at 850 °C. The formed crystals were analyzed using X-ray diffraction, whereas the resulting microstructures were quantified using scanning electron microscopy. During oxidation Ni is converted into NiO, and the latter interacts with Cr_2O_3 to form a $NiCr_2O_4$ spinel phase. Subsequent exposure to reducing conditions leads to an almost instantaneous decomposition of $NiCr_2O_4$ spinel, resulting in finely dispersed elementary Ni. This rearrangement of Ni by spinel decomposition leads to a significant improvement of the electrical conductivity of the Cr_2O_3 pellets compared to their initial state.

Keywords: solid oxide fuel cell (SOFC), $NiCr_2O_4$ (nickel chromate, spinel), metallic interconnects (MIC), oxide scale formation, Ni-mesh, metallic coating

1. Introduction

For stationary solid oxide fuel cell (SOFC) applications an average power degradation below 1 % per 1000 h operation over an minimal life time of 40,000 h is required [1–5]. Recent progress in SOFCs, particularly much improved anode redox stabilities [6, 7], has shifted research activities towards the reduction of the ohmic losses caused by oxide scales growing on metallic interconnects (MICs) [8–10].

Interconnects separate the fuel on the anode side from the air on the cathode side. They ensure proper gas distribution on the electrodes and collect and redistribute the electrical current from and to the cells, respectively [11–13]. Details about the various requirements imposed on interconnects of SOFC stacks and available materials are described elsewhere [11, 14, 15].

Significant losses are caused by Cr_2O_3 scale formation on Cr containing interconnects. This degradation occurs under both oxidizing and reducing (water containing) conditions [14]. Due to the low conductivity in the range of 0.001–0.2 $S\,cm^{-1}$ [17, 18], the oxide layers often provide a major contribution to the overall resistance of SOFC stacks. However, the extrinsic electrical conductivity of thermally grown semi-conductive Cr_2O_3 is influenced by various parameters including temperature, impurities and variations of the gas composition with the oxygen and water partial pressures as most relevant contributions. (Note: At temperature below 1000 °C the electrical conductivity of Cr_2O_3 is

*Corresponding author. Tel.: +41 58 934 7717; Fax: +41 58 934 7797

Email address: MarkusLinder@gmx.ch (Markus Linder)

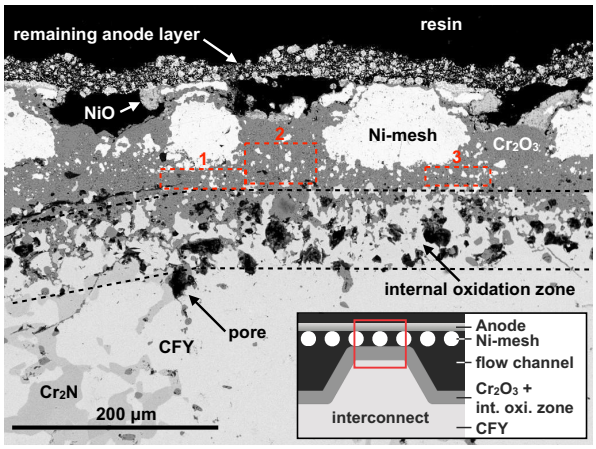

Figure 1: Cross section of a CFY MIC operated in a Hexis SOFC stack under real conditions at 900 °C for 40,000 h including 15 redox cycles running on CPOx reformed natural gas [14, 16].

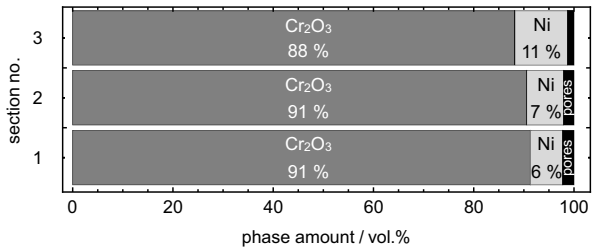

Figure 2: Phase distribution within thermal grown oxide scale after 40,000 h stack operation for the specific regions marked by red dashed rectangles in Fig. 1.

dominated by impurities, which is denoted as extrinsic property [18–22]). In our previous publication [15], we presented results for the ohmic losses originating from the cathode side of metallic interconnects. In this work, the focus will be on anodic side MIC degradation. As will be shown, the latter exhibiting greater variation in the microstructures, including possible formation of spinel phases. Additionally the extrinsic electrical conductivities may vary with changing gas composition. If Ni is present on the anode side of a SOFC stack repeat unit the formed Cr_2O_3 might interact with nickel or nickel oxide. The involved nickel might originate from different sources: the anode [23], the current-collector mesh [14, 24–26], or Ni-containing interconnect coatings [25, 27–30]. For a chromium based (CFY, [31]) interconnect operated for 40,000 h in a Hexis stack at about 900 °C, Fig. 1 shows a typical scanning electron microscopy (SEM) cross section. The image was taken at the top of the interconnect with a Ni-mesh and the remaining anode aside. The red rectangle in the inset illustrates schematically the SEM image location. Note the bright spots within the Cr_2O_3 matrix are identified as metallic Ni. Obviously, the Cr_2O_3 scale formed on the CFY MIC interacts with the Ni-mesh and the Ni containing anode. Note that the observed NiO represented as light gray color, was formed during shut down under partly oxidizing conditions. Dashed black lines mark the internal oxidation zone, which together with the Cr_2N formation are typical features of CFY degradation on the anode side [14]. To illustrate the magnitude of the local Ni content in a thermal grown Cr_2O_3 layer the phase content for three specific regions was additionally quantified within the red dashed rectangles in Fig. 1. The corresponding phase distributions are shown in Fig. 2. As shown the local Ni content can be rather high, i. e. more than 11 vol.%

It is obvious from Fig. 1 that the ohmic losses associated with oxide scales will depend in a complex way on the microstructure and the distribution of the various phases. In particular, it will depend on the presence of Ni, which has an electrical conductivity several orders of magnitude higher compared with that of Cr_2O_3 [17, 18, 32]. Therefore the motivation of this study is to improve the understanding of the Ni/Cr_2O_3 interaction typically occurring on the anode side of MICs with high chromium contents such as for CFY. Electrical conductivity measurements of MIC materials in reduced and/or oxidized gas atmospheres are indispensable to detect their overall degradation behavior. However, the obtained findings are difficult to interpret since they represent a superposition of a number of mechanisms such as oxide scale formation, segregation of reactive elements [33, 34], integration of impurities into the Cr_2O_3 lattice structure [19, 22, 35] and spinel formation by alloys. To single out the effect of Ni interaction with Cr_2O_3 we used instead pellets, which contained only Cr_2O_3, unavoidable pores and different amounts of Ni. The later one was systematically varied to take into account the observed wide range of local Ni contents in the anode side oxide scale as observed in Fig. 1. The electrical conductivities of these Ni containing pellets were studied in situ at different gas atmospheres including redox cycles for an overall period of more than 2000 h, i. e. under long-term conditions. In addition, the thermal activation energy was determined by temperature variations at different points in time. To allow more thorough interpretations, the obtained electrical conductivity denoted as σ_{eff} and the thermal activation energy E_{A} for all experimental data were complemented by microstructure, X-ray diffraction (XRD) and atomic force microscopy (AFM) data as well as information from literature.

Table 1: Ni content in Cr_2O_3 pellets and corresponding labels as used in this work. The test batch column denotes the two different conductivity measurement campaigns (cf. section 2.2).

sample #	Ni vol.%	matrix	text label	Fig. label	test batch #
1 2	0.0	Cr_2O_3	Cr_2O_3-0	0% Ni	2
3 4	0.5	Cr_2O_3	Cr_2O_3-0.5	0.5% Ni	1
5 6a 6b	5.0	Cr_2O_3	Cr_2O_3-5	5% Ni	1
7 8	10.0	Cr_2O_3	Cr_2O_3-10	10% Ni	1
9 10	20.0	Cr_2O_3	Cr_2O_3-20	20% Ni	2

2. Experimental details

2.1. Pellet preparation

To prepare the pellets, Cr_2O_3 powder was mixed with different amounts of nickel powder. The resulting compositions and the corresponding labels are summarized in Table 1. Note that the provided values for Ni content correspond to the volume fraction of solids e. g. a pellet with 10 vol.% Ni is denoted as Cr_2O_3-10. For the preparation of the Cr_2O_3-0.5 pellets Nickel(II) nitrate hexahydrate (N_2NiO_6 $6H_2O$) was mixed with the Cr_2O_3 powder. The samples with a Ni content of 5 vol.% and higher were admixed with ball milled metallic Ni particles with an averaged particle size r_{50} of 5.5 μm. To ease the pellet handling after pressing few drops Terpineol were added. The powder was uniaxially pressed with 200 kN at room temperature in a steel die with 40 mm diameter to form 2 mm thick tablets. The tablets were sintered in two batches at the highest available temperatures (for the available equipment) to minimize the porosity. The first batch with the Cr_2O_3-0 pellets was sintered in air for 2 h at 1585 °C. To avoid NiO formation the second batch with the Ni containing pellets was sintered for 2 h in reducing hydrogen atmosphere at 1400 °C, i. e. just below the Ni melting point. The tested Cr_2O_3 pellets of size 10–12 mm x 35 mm after sintering were cut out of the sintered tablets. Note that one Cr_2O_3-5 pellet was broken during preparation hence resulting in two smaller samples of sizes 5–7.5 $\times \approx$ 25 mm.

2.2. Electrical conductivity measurement

σ_{eff} was measured using a four-point probe set-up in a Gero SR 70-500 tube furnace under various atmospheres overall for more than 2000 h. To adjust the flow rates the set-up was equipped with flow controllers to overflow the samples with the desired atmosphere. The furnace was equipped with a Pt/YSZ/Pt-sensor to record the Nernst potential next to the samples. To monitor the temperature a thermocouple type K was also placed near to the samples. Since the used set-up did not provide measuring channels for all samples σ_{eff} characterization was done in two batches (cf. Table 1).

The testing procedure included long-term measurements at a fixed temperature of 850 °C and additional short-term temperature variations in the range of 750–950 °C to extract the corresponding thermal activation energies at selected points of time. The upper part in Fig. 3 schematically illustrates the different stages in varying atmospheres during long-term testing and the middle part shows the short-term temperature variation to determine E_{A} at different times. Fig. 3 shows in addition the corresponding temperature profile during the test procedure. More specific details about the applied gas compositions and temperatures during long- and short-term testing are given in Tables 2a and 2b, re-

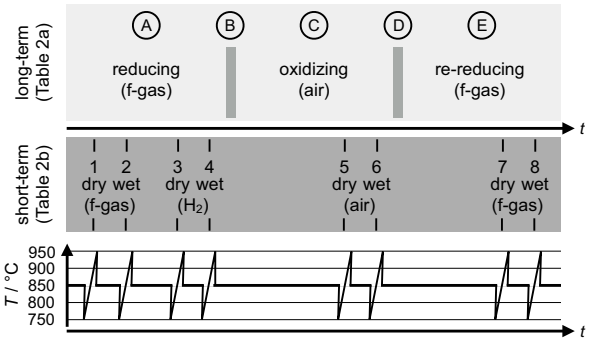

Figure 3: Schematic illustration of the varying atmospheres during testing. The upper part represents the five different stages during isothermal long-term testing at 850 °C. In particular, stages B and D denote the points in time of shifting from reducing to oxidizing atmospheres and vice versa. The middle part illustrates the short-term testing with applied temperature variations between 750 °C and 950 °C to extract the thermal activation energy E_{A}. The lower part illustrate the corresponding temperature profiles for both long- and short-term testing.

Table 2a: Summery of long-term test conditions with different atmospheres and specific gas compositions as illustrated in the upper part of Fig. 3.

stage	atmosphere	T / °C	gas label	gas composition	flow rate Nml min^{-1}
A	reducing	850	f-gas	5% H_2; 95% N_2	200
B	transition	850			
C	oxidizing	850	air	21% O_2; 79% N_2	200
D	transition	850			
E	reducing	850	f-gas	5% H_2; 95% N_2	200

Table 2b: Summery of short-term test conditions with different atmospheres and temperature variation ranges as illustrated in the middle part of Fig. 3.

T var no.	atmosphere	T / °C	gas label	humidity	gas composition	flow rate / Nml min^{-1}
1	reducing	750–950	f-gas	dry	5% H_2; 95% N_2	200
2				wet	4.8% H_2; 91.7% N_2; 3.5% H_2O	
3			H_2	dry	100% H_2	50
4				wet	96.1% H_2; 3.9% H_2O	
5	oxidizing	750–950	air	dry	21% O_2; 79% N_2	200
6				wet	20.3% O_2; 76.2 N_2; 3.5% H_2O	
7	reducing	750–950	f-gas	dry	5% H_2; 95% N_2	200
8				wet	4.8% H_2; 91.7% N_2; 3.5% H_2O	

spectively.

2.2.1. Long-term measurement

The long-term testing is done under isothermal conditions at 850 °C without additional humidification. σ_{eff} measurements were started in reduced forming gas (f-gas) atmosphere as denoted in the upper part in Fig. 3 by stage A. Note that details about all gas compositions and flow rates are given in Table 2a. Since the short time ranges during switching the gas compositions are also relevant for the interpretation of the results the shift from reducing to oxidizing conditions is denoted with stage B. The period where the samples were exposed to air for about 900 h is labeled as stage C and the transition from oxidizing back to reducing conditions as stage D. Finally, in stage E, the samples were again exposed to f-gas for about 900 h.

2.2.2. Short-term measurements, determination of activation energy E_A

The thermal E_A was determined by temperature variation (T var) at different time steps as shown in the lower part of Fig. 3. For this purpose, the temperature was increased in steps of 25 °C from 750 to 950 °C. The dwelling time for the short-term thermal activation tests was set to 45 min. To our experience, this time was sufficient to reach steady-state conditions. The thermal E_A was investigated in different gas atmospheres including humidification. Humidification is realized by rerouting the gas through a Perma Pure MH-110-12F-2 humidifier downstream to the furnace. With this equipment a humidification of 3–4 vol.% H_2O(g) is reached. During stage A, i. e. in reducing atmosphere, thermal E_A was determined in f-gas (T var 1), in humidified f-gas (T var 2), in hydrogen (T var 3) as well as in humidified hydrogen (T var 4). In oxidizing atmosphere (stage C) the temperature variations was performed in dry (T var 5) and humidified air (T var 6). Activation energies were again determined at the end of the test (stage E), i. e. after re-reduction using f-gas (T var 7), again without and with humidification (T var 8). All details about the applied gas compositions and corresponding flow rates during temperature variation are given in Table 2a.

2.3. Atomic force microscopy

AFM measurements were performed with a Bruker Multimode 8 (Karlsruhe) in PeakForce quantitative nano mechanical mode (QNM™). The nanomechanical properties were obtained by evaluation of a force distance curve performed at every contact point. Simultaneously to the topography, the electrical current was recorded using a PeakForce TUNA™ application module in tapping mode at an applied voltage of 1 V between tip and sample holder (tip at ground) and averaged by a lock-in amplifier. Further details on the measurement can be found in [36]. Furthermore, conductive PtIr-coated AFM probes (PPP-NCHPt (42 N m^{-1}; 330 kHz), Nanosensors™) were used. The investigated Cr_2O_3-20 pellet was glued onto a metallic AFM sample holder discs with conductive adhesive tape (Leit-C-Adhesive Tape, Plano).

2.4. Post test analysis

After the pellets have been cut out of the tablets the remaining materials were exposed to oxidizing and reducing conditions just as the pellets. At each sample removing point a small piece of these left overs was cut with a diamond disk for post test microstructure analysis.

In order to avoid artifacts from mechanical polishing [37], high quality cross-sections were produced by broad ion beam (BIB) polishing. For this purpose the

samples were fixed with resin on a 130 μm thick silica glass and polished with a Hitachi IM4000 broad ion beam (BIB) milling system. The parameters used for polishing are 1.5 kV accelerating voltage, 6 kV discharge, 30 swing angle and 2.5 h milling time. Scanning electron microscopy (SEM) images were taken with a Zeiss Gemini 1530 FEG with backscattered electron (BSE) detector.

X-ray diffraction (XRD) patterns were obtained on the cut surface of the Cr_2O_3-pellets with a Bruker D8 Advance. For this analyses Bragg-Brentano geometry with Ni-filtered Cu K_α radiation, constant illuminated sample-area, and a LynxEye position sensitive detector were used. The phases were identified by comparison with the ICDD database. For the figures presented in this publication, the contributions of the $K_{\alpha 2}$ radiation and the background were removed using the EVA (Bruker).

3. Results

The results section is structured as follows: First, the results from the long-term σ_{eff} measurements of the Cr_2O_3 pellets (with varying Ni contents) at 850 °C in various gas atmospheres are presented. Then, special focus is put on the changes of σ_{eff} during atmosphere switches, i. e. during stages B and D according to Fig. 3. The next section shows the results of the microstructure analysis for the Cr_2O_3 pellets with 10 and 20 vol.% Ni followed by the XRD patterns and the AFM data. Finally, the effect of temperature variation in various gas atmospheres and the corresponding thermal E_{A} are presented in Table 3. A comprehensive compilation of σ_{eff} values obtained at temperatures between 800 °C and 900 °C summarized in the supplementary in Table S1.

3.1. Long-term electrical conductivity of Cr_2O_3-pellets

Fig. 4 shows σ_{eff} data of the first batch of Cr_2O_3 pellets admixed with 0.5 vol.%, 5 vol.% and 10 vol.% Ni. Fig. 5 shows the corresponding results of the second batch for pure Cr_2O_3 pellets and those with 20 vol.% Ni. Note that σ_{eff} data for the initial reduction stage A have been omitted in both Figs. 4 and 5 because of the large scattering of the data during the temperature variations (T var 1–4) performed under this stage.

It can be observed that σ_{eff} of all samples shows a steep increase during stage B, i. e. when switching from reducing to oxidizing conditions. This increase takes place over a period of only a few hours. While exposed to air, i. e. during stage C, all Ni containing Cr_2O_3 pellets exhibit a further, but much slower increase in their

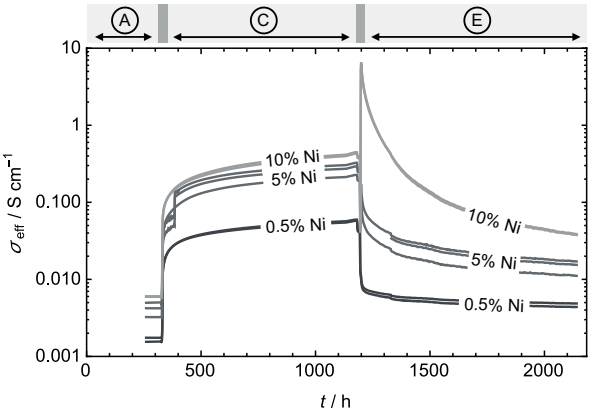

Figure 4: Electrical conductivity evolution of Cr_2O_3-0.5, Cr_2O_3-5 and Cr_2O_3-10 pellets measured at 850 °C in reducing f-gas and air. Data points for other temperatures (used for thermal activation energy E_{A} determination) were removed.

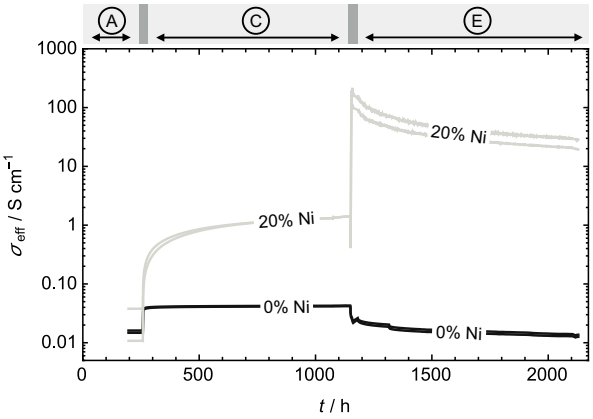

Figure 5: Electrical conductivity evolution of Cr_2O_3-0 and Cr_2O_3-20 pellets measured at 850 °C in reducing f-gas and air. Data points for other temperatures (used for thermal activation energy E_{A} determination) were removed.

σ_{eff} than during stage B. This is different, however, for the pure Cr_2O_3 samples, where σ_{eff} is constant in air. Switching back to reducing conditions, i. e. stage D, results in a "fast" decrease followed by an unexpected "fast" increase in σ_{eff} for the Cr_2O_3 pellets with Ni contents of 0.5 vol.% and higher. Both "fast" periods of decrease and increase last approximately 1–3 h. Again, the behavior of pure Cr_2O_3 without nickel is different in the sense that there is no increase of conductivity in the transition period at stage D. During the subsequent stage E in reducing atmosphere, all samples show a slow decrease in σ_{eff}. It is also important to note that the different responses of the sample properties (i. e. σ_{eff}) on the changing atmospheres (i. e. switching from reduced to oxidized and back) occur on different tempo-

Table 3: Thermal activation energy E_A data of sintered Cr_2O_3 pellets with different amounts of Ni determined under reduced and oxidized atmospheres. E_A were determined within a temperature range from 750 to 950 °C as shown in Figs. 15a and 16. Details about the used gas compositions are given in Tables 2a and 2b. Note, the corresponding electrical conductivity values reported in Table S1 were not corrected to eliminate the effect of nonzero porosities.

		stage A[a]				stage C[a]		stage D[a]	
		T var 1 f-gas dry	*T* var 2 f-gas wet	*T* var 3 H_2 dry	*T* var 4 H_2 wet	*T* var 5 air dry	*T* var 6 air wet	*T* var 7 f-gas dry	*T* var 8 f-gas wet
sample no.	Ni vol.%	E_A / eV	E_A / eV	E_A / eV	E_A / eV	E_A / eV	E_A / eV	E_A / eV	E_A / eV
1	0	1.038	0.744	0.937	1.051	0.264	0.265	0.882	0.888
2	0	1.008	0.709	0.904	1.016	0.253	0.253	0.854	0.866
3	0.5	1.099	1.056	1.110	1.037	0.252	0.247	0.945	0.818
4	0.5	1.112	1.065	1.135	1.072	0.243	0.235	0.953	0.809
5	5	0.874	0.640	0.957	0.695	0.188	0.187	0.799	0.755
6a	5	-	-	-	-	0.188	0.190	0.990	0.761
6b	5	0.980	0.755	1.058	0.867	0.202	0.204	0.861	0.654
7	10	0.893	0.797	0.971	0.794	0.214	0.211	0.933	0.723
8	10	0.951	0.838	1.005	0.818	0.219	0.217	0.958	0.755
9	20	1.024	0.717	1.012	1.093	0.190	0.187	-0.080	-0.052
10	20	1.057	0.748	1.066	1.155	0.204	0.203	-0.064	-0.058

[a] details about the different stages are given in Fig. 3 and section 2.2.1, respectively.

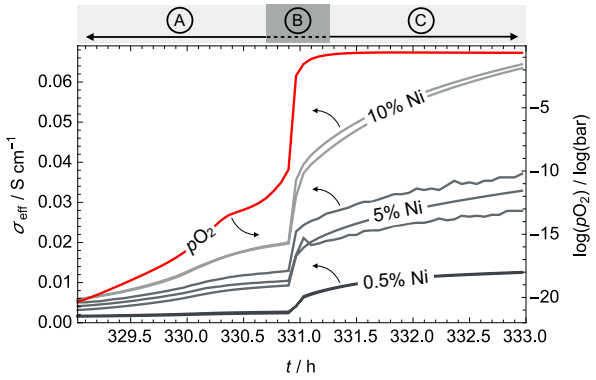

Figure 6: Electrical conductivity data of the first batch with Cr_2O_3-0.5, Cr_2O_3-5 and Cr_2O_3-10 during change from reducing forming gas (95 % N_2, 5 % H_2) atmosphere to air at 850 °C. The red curve shows the corresponding oxygen partial pressure based on the measured Nernst potential. Note, the tentative pO_2 increase after atmosphere change is related to some technical issues with the applied mass flow controller.

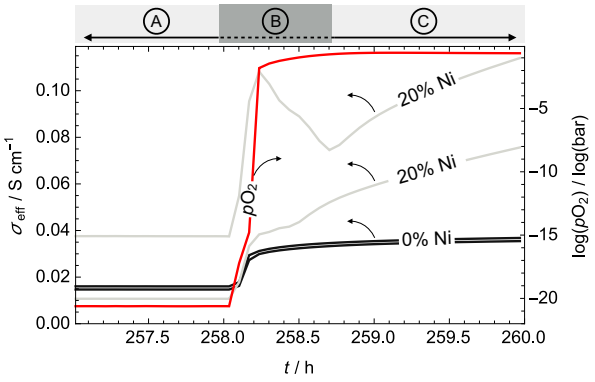

Figure 7: Electrical conductivity data of the second batch with Cr_2O_3-0 and Cr_2O_3-20 during change from reducing forming gas (95 % N_2, 5 % H_2) atmosphere to air at 850 °C. The red curve shows the corresponding oxygen partial pressure based on the measured Nernst potential.

ral lengths scales: some take place within few hours, others expand over hundreds of hours. This behavior is explained in section 4. These measurements clearly demonstrate that the addition of Ni has a strong effect on σ_{eff} when compared with the results of the pure Cr_2O_3 pellets.

Stage E shows the re-reduction in f-gas. The Cr_2O_3-10 and Cr_2O_3-20 pellets show a sharp increase of σ_{eff} after changing the atmosphere from air to f-gas (stage D). Subsequently to this temporary increase σ_{eff} is continuously decreasing. In summary, the total decrease of σ_{eff} upon re-reduction in stage E is less pronounced compared to the increase upon oxidation (stages B, C) and the fast increase upon reduction (stage D). This leads to an overall increase of σ_{eff} by up to one order of magnitude. The sample without Ni does not show this improvement and its conductivity turns back to the initial level after re-reduction.

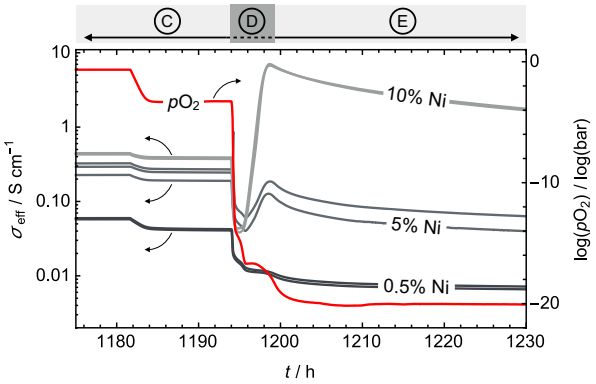

Figure 8: Change from air to reducing forming gas (95 % N_2, 5 % H_2) atmosphere and corresponding electrical conductivity σ_{eff} behavior of Cr_2O_3 pellets admixed with Ni particles measured within the first batch. The red curve shows the corresponding oxygen partial pressure based on the measured Nernst potential. Note, the pO_2 plateau at 10^{-4} bar is related to technical issues with the applied mass flow controller during atmosphere switch form air to f-gas.

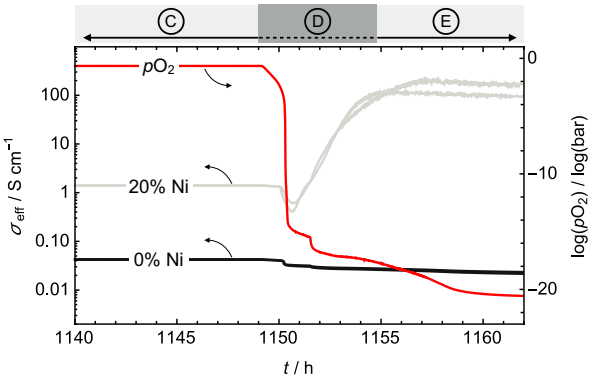

Figure 9: Change from air to reducing forming gas (95 % N_2, 5 % H_2) atmosphere and corresponding electrical conductivity σ_{eff} behavior of Cr_2O_3 pellets admixed with Ni particles measured within the second batch. The red curve shows the corresponding oxygen partial pressure based on the measured Nernst potential.

3.2. Electrical conductivity behavior during atmosphere change

As pointed out above, changing the gas atmosphere from reducing to oxidizing conditions and back again has a profound impact on σ_{eff} of the Cr_2O_3 pellets. These changes in σ_{eff} become more pronounced with increasing Ni contents. To further highlight the conductivity behavior during the transitions from one gas atmosphere to another, Figs. 6–9 provide further details. Figs. 6 and 7 provide details of the changes in σ_{eff} when going from reducing f-gas to air. Similarly, changing from air back to f-gas is shown in detail in Figs. 8 and 9. In addition to the provided σ_{eff}, all diagrams show the corresponding oxygen partial pressures as obtained from measuring the Nernst potential. Figs. 6 and 7 provide a clear trend: σ_{eff} shows an abrupt rise within few minutes after switching from f-gas to air. This is followed by a much slower, continuous increase. This behavior is more pronounced at higher Ni content. Note also that one of the samples with 20 vol.% Ni deviates from the behavior described above. There, right after switching the gas composition, the steep increase is followed by a short decrease (over about half an hour), followed again by a slow increase in σ_{eff}. Moreover the oxygen partial pressure follows the behavior observed for σ_{eff}. However, after stage B, it reaches a constant value much more quickly.

Figs. 8 and 9 highlight the changes in σ_{eff} when switching back from air to f-gas. During the transition (stage D) the evolution of the pO_2 is discontinuous. Obviously the reduction of the samples influences or buffers somehow the pO_2 in the furnace. This is accompanied by a decrease in the oxygen partial pressure. After reaching a $pO_2 < 10^{-17}$ bar, σ_{eff} increases significantly for Cr_2O_3 pellets containing ≥ 5 vol.% Ni. After reaching a maximum at $pO_2 \approx 10^{-18}$ bar σ_{eff} decreases again. Note also that the Cr_2O_3-0.5 pellets show a stagnation in σ_{eff} at a pO_2 of around 10^{-17} bar, which is also visible in the pO_2 curve. A similar trend in the pO_2 behavior can be observed in Fig. 9.

3.3. Microstructure analysis of Cr_2O_3 pellets

SEM images of a Cr_2O_3-10 pellet polished with BIB are shown in Fig. 10. The horizontal direction gives the microstructure evolution at three different instants of time, i. e. at 300 h (stage A, f-gas), at 1200 h (stage C, air), and at 2150 h (stage E, f-gas). In the vertical direction, the magnification level increases from the top to the bottom line. Figs. 10a, 10d and 10g show the initial microstructure in f-gas atmosphere for three different magnification levels. The admixed Ni particles are evenly distributed within the Cr_2O_3-matrix. Sharp transitions between the two solid phases can be observed. The Ni particle sizes are still similar to the original particle sizes ($r_{50} = 5.5\,\mu$m) as admixed to the Cr_2O_3 powder.

After being exposed to air for 550 h the microstructure significantly differs from the original one. At the lowest magnification the Ni particles appear to be blurred, compare Figs. 10b with 10a. At higher magnifications shown in Figs. 10e and 10h the Ni particles were as expected oxidized and they fill up additional pore space due to the associated volume increase. Furthermore, the formation of a $NiCr_2O_4$ spinel took place, as confirmed by XRD patterns presented in section 3.4. Note that the different oxide phases (NiO,

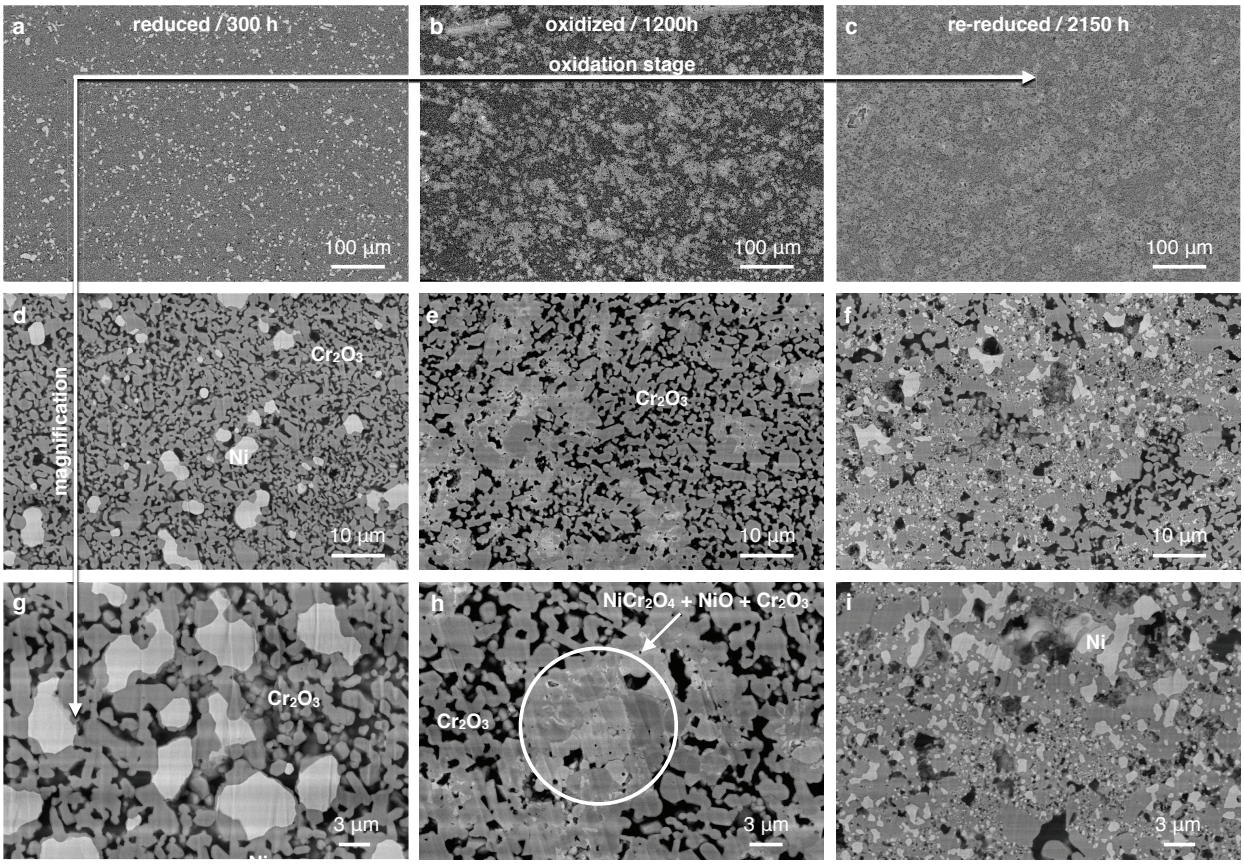

Figure 10: Microstructures of Cr_2O_3 pellets with 10 vol.% Ni prepared by BIB after different test steps in reduced and oxidized atmosphere at 850 °C are shown in the columns. The time specification denotes the approximated furnace removal corresponding to Fig. 4. Increasing magnifications of Cr_2O_3 pellets section are shown from top to bottom. In reduced state in g) and i) two clearly separated solid phases i. e. Cr_2O_3 and Ni can be observed. In oxidized state the contrast between different phases including Cr_2O_3, NiO and $NiCr_2O_4$-spinel is very low. The black phase represents the pore

Cr_2O_3, $NiCr_2O_4$) have similar backscatter coefficients and hence the contrast in SEM is poor for the oxidized samples.

Re-reducing, i. e. exposing the samples again to the low pO_2 f-gas, leads to further microstructure transformations as shown in Figs. 10c, 10f and 10i. Under these conditions NiO and $NiCr_2O_4$ spinel are completely dissolved. Interestingly, the resulting Ni shown in Figs. 10f and 10i is finely dispersed into smaller particles with diameters of less than 1 μm. In addition the small black dots of similar sizes, which can be observed in these domains represent micro pores.

Fig. 11 provides examples of the microstructures of the Cr_2O_3-20 pellets at the beginning and at the end of stage E, i. e. after being again reduced in f-gas for 12 h and 900 h, respectively. Comparing Fig. 11a with Fig. 11b a general smoothing of the contours of the Ni particles can be observed.

The porosity of the samples was determined after sintering based on the weights and volumes of the pellets. The Cr_2O_3-5, Cr_2O_3-10 and Cr_2O_3-20 samples showed a porosity of around 36 %. The Cr_2O_3-0.5 samples exhibited a porosity of 44 %. The porosity of the Cr_2O_3-0 pellets was 27 %, as obtained from post test SEM images analysis. Note, that the rather large porosity of the analyzed pellets has a significant effect on the obtained σ_{eff}. Consequently, the obtained σ_{eff} will be generally lower than those for oxide scales thermally grown on metallic interconnects under typical SOFC stack operation conditions. Note also that the obtained σ_{eff} data and corresponding thermal E_{A} were not corrected to eliminate the effect of the pores. The reason is that the Cr_2O_3 pellets admixed with Ni contain two different electron conducting phases that cannot be simply corrected for pore effects, e. g. by Archie's law or by other recently published methods [38–40].

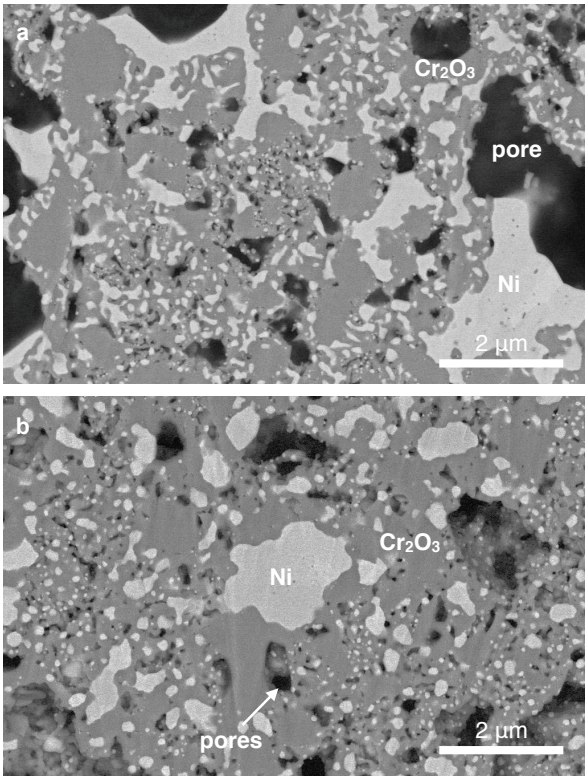

Figure 11: a) Microstructure of Cr_2O_3 pellet with 20 vol.% Ni immediately (12 h) after atmosphere change from air to re-reduction in f-gas at 850 °C and b) after re-reduction in f-gas for about 900 h.

3.4. XRD data

XRD of sintered Cr_2O_3 pellets with 10 and 20 vol.% Ni were studied at different stages of the long-term experiments. Fig. 12 shows the results for the Cr_2O_3-10 pellets at the end of stage A in f-gas, during stage C in air and at the end of stage E in f-gas. Note that Cr_2O_3 diffraction peaks were present in all analyzed samples. Furthermore, from the pattern in Fig. 12a Cr_2O_3 and Ni can be identified after being exposed to f-gas for 320 h. As shown in Fig. 12b being exposed to in air for 550 h NiO and $NiCr_2O_4$ spinel can be identified. Finally, after re-reduction in f-gas for 900 h the previously formed NiO and $NiCr_2O_4$ spinel cannot be retrieved anymore in the XRD pattern shown in Fig. 12c.

Fig. 13 shows the XRD patterns for the Cr_2O_3-20 pellets after oxidation in air at the end of stage C and after re-reduction in forming gas for ca. 12 h i. e. at the end of stage D, respectively. The XRD pattern in Fig. 13a shows that the $NiCr_2O_4$ spinel and NiO phases are present after being exposed to air. These two phases cannot be detected anymore in Fig. 13b after short re-reduction using f-gas. However, metallic Ni

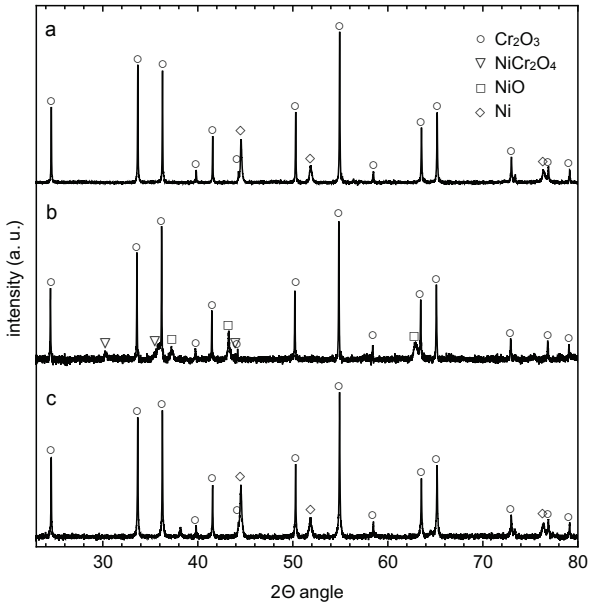

Figure 12: XRD patterns of Cr_2O_3 pellets with 10 vol.% Ni after heat exposure in different atmospheres at 850 °C. a) after exposure to reduced forming gas (95 % N_2, 5 % H_2) removed after 320 h, b) after exposure to air for 550 h and c) after re-reduction in forming gas for another 900 h.

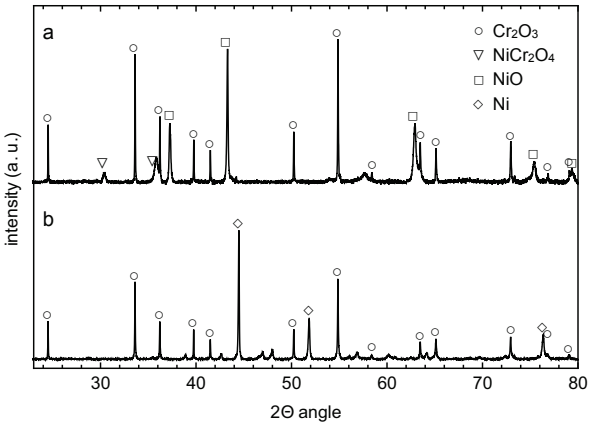

Figure 13: XRD patterns of Cr_2O_3 pellets with 20 vol.% Ni after heat exposure in different atmospheres at 850 °C. a) after exposure to air for 850 h and b) after re-reduction in forming gas for 12 h. Note that the non-marked peaks in b) originate from the sample holder ($CaCO_3$).

could be verified in this XRD pattern.

3.5. AFM data

In Fig. 14 AFM images of a Cr_2O_3-20 pellet as sintered in reducing atmosphere are shown with a) surface topography, b) feedback signal, c) electrical current transition (bright spots) and d) the electrical current profile along the marked red line in c) are shown.

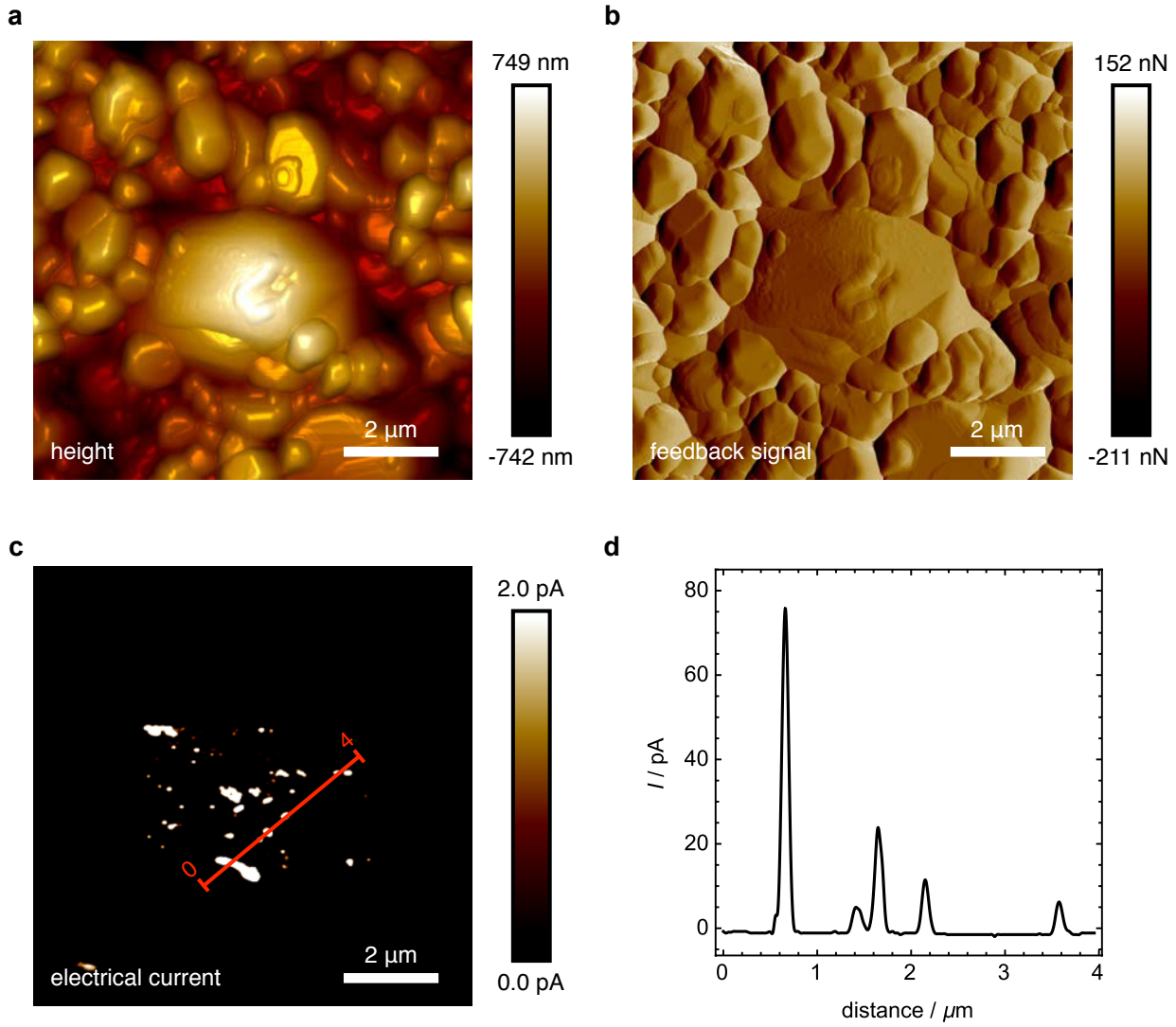

Figure 14: AFM images of a Cr_2O_3-20 pellet after sintering with a) topography information, b) feedback signal, c) binarized electrical current flux (bright spots) and d) section of the effective electrical current along the red line in image c).

The height image in Fig. 14a shows the topography of the sample. In the feedback regulation signal in Fig. 14b sharp height changes are recorded to enhance the surface structures. The current is measured during contact of the tip with the sample and averaged using a lock-in-amplifier. Numerous grains with an area from approximately $0.065\,\mu m^2$ up to approximately $11.561\,\mu m^2$ are visible. The large grain in the center is locally electrically conductive at room temperature as shown in Fig. 14c. This indicates that the admixed Ni forms some percolating paths across the pellets. In the current profile in Figure Fig. 14d single conductive spots with a maximum current of approximately 80 pA were measured. Note, the scale in Fig. 14c is purposely limited to 2 pA to visualize electrical conductive spots i. e. to display it as a binarized electrical conductivity map. Thus the most part of the sample is not electrically conductive at room temperature. 3D-topography overlaid with adhesion force and electrical current data, respectively from a different sample location are shown in the supplementary Fig. S1.

3.6. Temperature dependence of electrical conductivities

Temperature variations between 750–950 °C were applied to determine the thermal E_A based on σ_{eff} of the various Ni-containing Cr_2O_3 pellets at different stages

of the long-term experiments. The scatter of the experimentally determined σ_{eff} for the pellets with the same Ni amount is in general small i. e. 0–30 %. It is suggested that the observed deviations are related to some variances in the pellet dimension and measured distance between the voltage taps. Stage A included measurements T var 1–4 to determine the thermal E_{A} in f-gas and pure hydrogen, both either dry or additionally humidified with 3–4 vol.% water. σ_{eff} determined in stage A at 850 °C are in the range of 0.0012–0.0715 S cm^{-2}. σ_{eff} data from measurement T var 1 in dry f-gas are shown as an Arrhenius plot in Fig. 15a. All samples follow in good approximation a straight line in Arrhenius form with similar slopes resulting in thermal E_{A} between 0.873–1.112 eV. Samples with a higher amount of Ni generally have an increased σ_{eff} except for the Cr_2O_3-0 pellets, which are in the range of the Cr_2O_3-20 pellets. This behavior is attributed to different sintering conditions as will be discussed in section 4.1.1.

The data in Table S1 show that humidification of both f-gas and hydrogen leads to an increase of σ_{eff} compared to the results in dry reducing atmospheres. Note that the influence of humidity is less pronounced in H_2 than in f-gas where compared to dry f-gas the thermal E_{A} is reduced by humidification (cf. Table 3). However, in pure hydrogen no clear trend could be observed for the thermal E_{A} resulting from dry and humidified atmospheres. At the end of stage C the thermal E_{A} was determined in T var 5 for dry and at T var 6 for humidified air. The corresponding data in Table S1 shows that σ_{eff} is not really affected by humidification of air. Furthermore, the thermal E_{A} for dry (0.187–0.265 eV) and humidified air (0.188–0.264 eV) are similar. The temperature dependence of σ_{eff} at the end of stage E in dry f-gas atmosphere are shown in Fig. 16 (T var 7). In addition, the results of the corresponding data in wet f-gas are given in Table 3 and Table S1, respectively. Finally, Arrhenius plots for all performed temperature variations are given in the supplementary in Figs. S2–S5. It can be seen that σ_{eff} is increased in humidified atmosphere compared with dry. Except for the Cr_2O_3-20 pellets, which show a decreased σ_{eff} in humidified atmosphere after stage E resulting in thermal E_{A} value of -0.079 eV and -0.064 eV, respectively. Also, the thermal E_{A} in humidified f-gas is smaller compared to that in dry f-gas. The two Cr_2O_3-20 pellets show again a diametrically opposed behavior. A general comparison of the thermal E_{A} energies show that those in oxidizing atmosphere (T var 5 and 6) are 4–5 times higher compared to those in reducing atmosphere (T var 1–4,7 and 8). Humidification and variation in the gas composition, i. e. f-gas versus pure H_2 do not influence the thermal activation significantly.

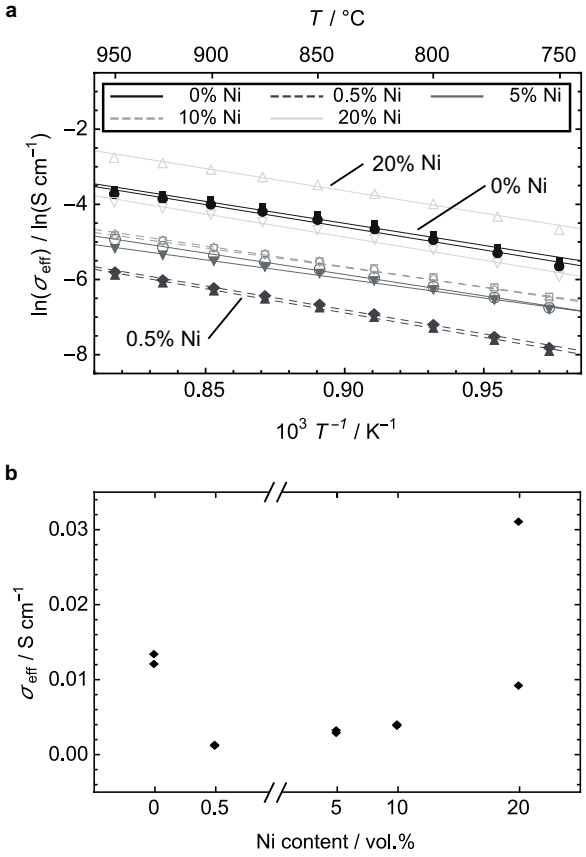

Figure 15: a) Arrhenius plot of the electrical conductivities σ_{eff} of the investigated Ni containing Cr_2O_3 pellets in reducing f-gas atmosphere without humidification. The temperature variation was done within the first 100 h after startup. The corresponding E_{A} values are given in Table 3. b) Corresponding σ_{eff} plotted as a function of Ni content obtained at 850 °C.

4. Discussion

This section is structured according to stages A–E of the performed long-term conductivity measurements, see Fig. 3. The measured σ_{eff} are discussed in detail, taking into account the applied gas atmospheres and the additional SEM, XRD and AFM data. Based on these experimental results, several microscopic mechanisms are proposed to explain the observed complex and partly counterintuitive time-dependencies of the obtained σ_{eff} data. Furthermore, the presented subsections are further subdivided into i) changes in the microsturcture of the Ni containing Cr_2O_3 pellets that affect the overall electrical conductivity and ii) effects related to the extrinsic electrical conductivities of the Cr_2O_3 phase. The

temperature dependencies of the obtained σ_{eff} data and associated thermal E_{A} are discussed at the end of this section.

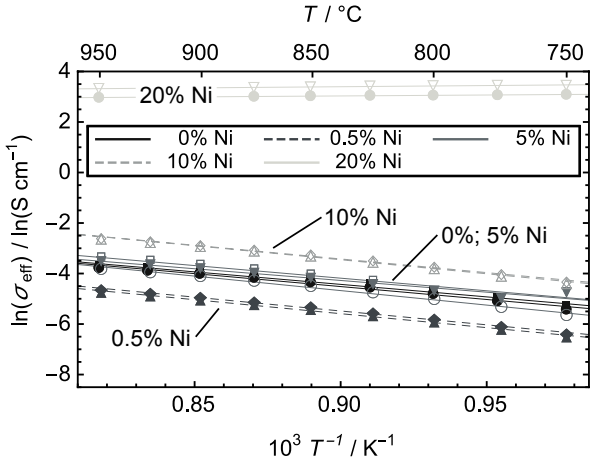

Figure 16: Arrhenius plot of the electrical conductivities σ_{eff} of the investigated Ni containing Cr_2O_3 pellets at the end of stage E in dry f-gas atmosphere. The corresponding E_{A} values are given in Table 3.

4.1. Electrical conductivities at stage A in reducing atmosphere

σ_{eff} behavior during stage A is shown in Figs. 4 and 5. After sintering and equilibration at constant reducing atmospheres the σ_{eff} of all samples is also constant, but it depends greatly on the Ni-content of the samples. Explanations of the underlying mechanisms are provided in the following subsections.

4.1.1. Microstructure effects

σ_{eff} of the Cr_2O_3 pellets with admixed Ni particles is significantly influenced by the amount of Ni as shown in Fig. 15 and Table S1. In general the electrical conductivity increases with the Ni content.

Representative microstructures of a Cr_2O_3-10 pellet after sintering and exposure to f-gas are shown in Figs. 10a, 10d and 10g. Note that the metallic Ni particles are in contact with the Cr_2O_3 and with additional pores, see Fig. 10d and 10g. Since at the considered temperatures the electrical conductivity of Ni [32] is several orders of magnitudes higher than that of Cr_2O_3 [15, 17, 18, 35, 43, 44] it is obvious that electrical current paths within the Ni particles are preferred over those within the Cr_2O_3 phase. This behavior is schematically illustrated in Fig. 17a. The arrows indicate preferred electrical current paths across the Ni particles. Since the Ni particles generally do not percolate

Table 4: Summary of intrinsic electrical conductivities of the various phases.

material	σ / S cm^{-1}
Cr_2O_3 at 850 °C [15, 17, 18, 35, 43, 44]	< 0.1
Ni at 0 °C [32]	> 100,000
$NiCr_2O_4$ at 850 °C [45]	0.63
NiO at 850 °C [46, 47] and at 1000 °C [48]	0.1

especially for pellets with low Ni contents, the electrical properties of the Cr_2O_3 matrix still limits the overall electrical behavior within the compacts.

Ni percolation can be expected starting roughly from about 20 vol.%. This might explain the rather large difference by a factor of 3 between σ_{eff} of the two considered Cr_2O_3-20 pellets. This deviation might be related to some partly percolated Ni paths within the two samples since the deviation for the Cr_2O_3 pellets with less Ni is determined in the range of 0–30 %. AFM data in Fig. 14 provides additional evidence for this type of behavior. It shows such percolating Ni paths in through direction obtained at room temperature by electrical potential measurements.

An additional microstructure effect is associated to the differences in the sinter conditions for the Cr_2O_3-0 pellets, as mentioned in section 2.1. The Cr_2O_3-0 pellets were sintered at higher temperature of 1585 °C compared to the Cr_2O_3 pellets with Ni ≥ 0.5 vol.% that were sintered at 1400 °C. As a result of the higher sinter temperature the Cr_2O_3-0 pellets exhibits a lower porosity, which improves σ_{eff} compared with that over the higher porosity Ni containing pellets.

4.1.2. Electrical conductivity of Cr_2O_3 phase

In samples where the Ni-content is below the percolation threshold all transport pathways lead partially or fully through the matrix of Cr_2O_3. The conductivity of Cr_2O_3 is thus the limiting phase for charge transport in these samples. From literature it is known that the conductivity of Cr_2O_3 varies greatly between 0.001 and 0.2 S cm^{-1} [17, 18]. Its conductivity is greatly dependent on the defect density. In the following we briefly discuss the most important mechanisms of defect formation in Cr_2O_3 and the relationship with pO_2.

It is widely accepted that Cr_2O_3 is a p-type semiconductor. It has been suggested that the relevant defects for p-type conductivity are related to Cr vacancies, formulated by the Kröger-Vink notation, according to

$$\tfrac{3}{2}\,O_2 \quad = \quad 3\,O_O + 2\,V_{Cr}''' + 6\,h^{\bullet} \quad \text{[19, 20, 49–51]}. \quad (1)$$

Note that Eq. (1) introduces a pO_2 dependency of the vacancies and of the associated electrical conductivity,

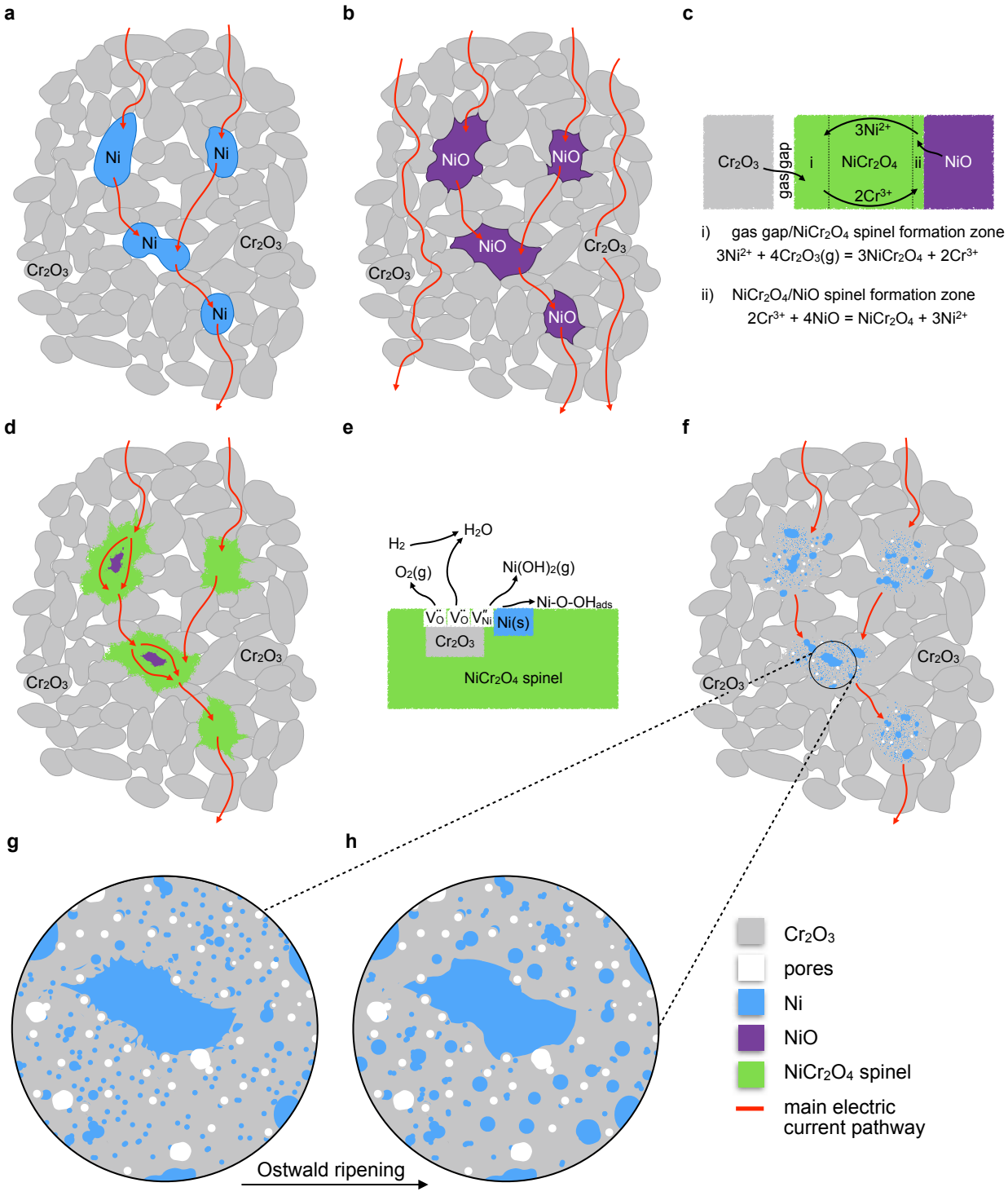

Figure 17: Microstructure changes during the evolution of the Ni containing Cr_2O_3 pellets under reducing, oxidizing and re-reducing conditions. a) initial microstructure at stage A with metallic Ni. b) NiO formed during change from f-gas to air at stage B. c) $NiCr_2O_4$ spinel formation mechanism [41, 42] during oxidation in air at stage C. d) Cr_2O_3 matrix with formed spinel and remaining NiO at the end of stage D. e) $NiCr_2O_4$ spinel decomposition mechanism during change from air again to f-gas at stage D. f) finely dispersed Ni after spinel decomposition at the beginning of stage E. g) and h) show the rearrangement and smoothing of small Ni particles during stage E by Ostwald ripening.

which will be considered again in the discussion of the later stages. It has also been reported in the literature that the defect structure of a Cr_2O_3 phase can change at low oxygen partial pressures [52, 53]. Consequently, the electrical conductivity behavior can change from p-type to a n-type. Such a process was observed for Cr_2O_3 by Matsui and Naito [52] for pressures between 10^{-8} and 10^{-13} bar in a H_2/CO_2 atmosphere. Since the oxygen pressure is even lower in the applied f-gas atmosphere ($pO_2 \approx 10^{-20}$ bar) the defect mechanism might be related to an oxygen release accompanied by the formation of oxygen vacancies

$$O_O = V_O^{\bullet\bullet} + 2\,e' + \tfrac{1}{2}\,O_2 \quad [44, 50, 54]. \qquad (2)$$

These very low pO_2 can also be observed under typical SOFC stack operation conditions on the anode side ($pO_2 < 10^{-14}$ bar [55]). Park and Natesan [44] investigated the electrical conductivity of thermally grown Cr_2O_3 for temperatures below 1000 °C and for pO_2 near the decomposition pressure of Cr_2O_3 ($pO_2 < 10^{-24}$ bar) in a gas-tight cell. They only found a gradual decrease of electrical conductivity with decreasing oxygen partial pressure.

At the investigated temperatures below 950 °C the electronic defect concentration is assumed to be small, which indicates that the electrical conductivity of Cr_2O_3 is essentially influenced by impurities [17, 19, 21, 35, 43, 49, 50, 54, 56]. Impurities are side effects, which cannot be prevented neither in compacts produced in the laboratory nor in thermally grown oxide scales. A proposed defect mechanism for impurities is given by

$$2\,AO + \tfrac{1}{2}\,O_2 = 2\,A'_{Cr} + 3\,O_O + 2\,h^{\bullet} \quad [21, 50] \quad (3)$$

where A represents an impurity atom. However, for oxide layers formed on metallic interconnects during SOFC stack operation, such impurities are highly beneficial since they decrease the ohmic resistances. Overall, it must be emphasized that the defect structure of Cr_2O_3 is difficult to determine experimentally [51] and is only considered on a theoretical basis in this discussion.

The relatively high σ_{eff} of the Cr_2O_3-0 pellets (see Fig. 15) is on the one hand related to the microstructure as discussed in section 4.1.1 and on the other hand to the incorporation of different types of defects, which result in different defect densities in the Cr_2O_3 matrix. This defect incorporation can be associated to the sinter condition due the fact that the Cr_2O_3-0 pellets were sintered in air at 1585 °C whereas the Cr_2O_3 pellets with Ni ≥ 0.5 vol.% were sintered in reducing hydrogen atmosphere at 1400 °C. Dependencies of the electrical properties of Cr_2O_3 compacts on the sintering conditions also have been reported by Young et al. [53]. Note that σ_{eff} most probably is affected by a superposition of both microstructure (see section 4.1.1) and defect effects. Since the influence of varying sinter conditions and its effect on the porosity and hence electrical conductivity is not specifically addressed in this work the absolute deviations of σ_{eff} between the Cr_2O_3-0 and the Ni containing pellets are not discussed. Instead the observed behavior for the Cr_2O_3-0 pellets is used as a reference to explain the response in the electrical conductivity during atmosphere changes.

4.2. Electrical conductivities at stage B during change from reducing to oxidizing atmosphere

4.2.1. Microstructure effects

Another aspect that influences σ_{eff} of the Cr_2O_3 pellets is related to the oxidation of metallic Ni into NiO at a given temperature in air. Ni reacts with gaseous oxygen to form NiO on the surface of the original Ni particles. A high defect concentration in the NiO crystal lattice promotes a fast and complete oxidation of Ni at 850 °C [57]. This transformation of Ni to NiO leads to an alteration of the microstructure, which is schematically illustrated in Fig.17b. The oxide tends to fill the pores in the vicinity of the original Ni particles, since the formation of NiO comes along with a significant volume increase of 69.9 % [58].

The electrical conductivity of NiO is significantly smaller compared to that of metallic Ni [32, 46, 48] (cf. Table 4). Therefore, it can be ruled out that the observed fast increase in σ_{eff} during stage B is related to the formation of NiO. As pointed out above, NiO has a much lower electrical conductivity than Ni which results in a decrease of the overall conductivity of the pellet, if the effective conductivity is dominated by charge transport in the Ni phase. Such a decrease in σ_{eff} can be clearly identified in Fig. 7 for one of the Cr_2O_3-20 pellets. This pellet already showed in f-gas a more than three times higher σ_{eff} compared to the other one with the same Ni amount. The decreasing conductivity during stage B/beginning of stage C for one sample with 20 vol.% Ni can thus be attributed to a loss of percolation in the Ni phase upon transformation of Ni into NiO.

This transformation results in well pronounced transitions of σ_{eff} within 0.5 h after switching to air. However, this identified Ni oxidation time differs from those given in literature [59, 60] for the following reasons: the admixed Ni with $r_{50} = 5.5\,\mu m$ contains also some smaller Ni particles, which results in faster complete oxidation. The observed behavior for the Cr_2O_3-20 pellets can be related to a superposition of Ni oxidation and the initial $NiCr_2O_4$ spinel formation, which provides new

preferred electrical current pathways along the spinel phase, see Fig. 17d.

4.2.2. Electrical conductivity of Cr_2O_3 matrix

σ_{eff} behavior during switching from f-gas to air is shown in Figs. 6 and 7. This change of gas atmosphere results in a fast and significant increase of σ_{eff} during stage B followed by a slower, exponential increase in stage C (discussed in section 4.3). The degree of conductivity change in phase 3 clearly correlates with the Ni content, whereas in phase 2 this correlation is not clear. The sharp increase of σ_{eff} in stage B can be assigned to the increase of the extrinsic electrical conductivity of the Cr_2O_3 matrix at higher oxygen partial pressure [44, 52]. This effect should be largely independent from the Ni-content. Suppose the defect structure is described according to Eq. (1) thermodynamic equilibrium then yields to the relation

$$\sigma \propto p_{O_2}^{3/16} \tag{4}$$

i. e. the electrical conductivity σ is proportional to the oxygen pressure by the power of 3/16 [17, 19, 20, 44, 61]. If impurities are involved thermodynamic equilibrium for Eq. (3) would yield to

$$\sigma \propto p_{O_2}^{1/8} \quad [21]. \tag{5}$$

For n-type defects in low pO_2 atmospheres as described in Eq. (2) the following pressure dependence is obtained

$$\sigma \propto p_{O_2}^{-1/6} \quad [51]. \tag{6}$$

In this case the electrical conductivity decreases due to the negative exponent. In this study, the pO_2 dependency was not established on a quantitative level, since conductivity measurements were not performed under systematic pO_2 variations, but only at two levels (either air or f-gas).

4.3. Electrical conductivities at stage C in oxidizing atmosphere

A continuous increase of σ_{eff} can be observed for the Ni containing pellets in the oxidizing air environment from Figs. 4 and 5. This is even more pronounced in Fig. 18 where the relative increase of σ_{eff} is plotted as a function of time. This demonstrates that the relative increase of σ_{eff} is increasing with the Ni amount. The strong deviations between the two Cr_2O_3-20 samples can be explained by the fact that at 20 vol.% Ni the percolation limit is reached.

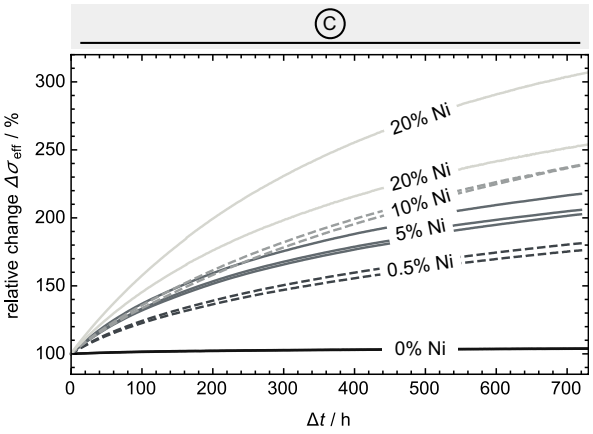

Figure 18: Relative increase of electrical conductivity σ_{eff} during oxidation in air at 850 °C for all tested samples. For better comparison of the relative changes in σ_{eff} the starting point was defined several hours after the switch to oxidizing atmosphere.

4.3.1. Microstructure effects

The improvement of σ_{eff} for the Ni containing pellets can be related to the formation of $NiCr_2O_4$ spinel as shown in Fig. 17d. The electrical conductivity of $NiCr_2O_4$ is higher compared to those of Cr_2O_3 and NiO [45, 47] (cf. Table 4) As a consequence a higher Ni content leads to more pronounced formation of $NiCr_2O_4$ spinel and therefore also to a stronger increase of σ_{eff}. Electrical conductivity in the spinel phase is generally explained by electron hopping and by the associated changes in the valence state of Cr. The formation of $NiCr_2O_4$ spinel at the expense of metalic Ni could be verified by XRD as shown in Figs. 12b and 13a. In the same XRD patterns some remnants of NiO could also be identified. Based on this observation it becomes evident that the spinel formation is not completed within the investigated period of about 900 h. However, based on the available data it can be estimated that the asymptotic behavior for σ_{eff} would be achieved within additional 500 h of exposure to air.

Fig. 17c illustrates the mechanism of spinel formation, which is initiated at the interface beween Cr_2O_3 and NiO phase according to

$$Cr_2O_3 + NiO \quad = \quad NiCr_2O_4. \tag{7}$$

After the initial formation of a first spinel phase between Cr_2O_3 and NiO the subsequent spinel formation takes place at the two new interfaces (i. e. Cr_2O_3/$NiCr_2O_4$ and $NiCr_2O_4$/NiO). As a consequence, further spinel formation depends on ionic counter diffusion within the spinel. A schematic illustration of the spinel formation mechanism within the Cr_2O_3 matrix is given in

Fig. 17c [41, 62]. Cr_2O_3 is transported via the gas phase (e. g. by CrO_3 and/or $CrO_2(OH)_2$ [63]) to the reaction zone at the $NiCr_2O_4$ spinel interface [41, 42, 64]. Gas phase transport is more likely since the contact between Cr_2O_3 and $NiCr_2O_4$ is imperfect, i. e. at best there exist some isolated contact areas [64]. The reaction at the Cr_2O_3/$NiCr_2O_4$ interface can be written as

$$3\,Ni^{2+} + 4\,Cr_2O_3(g) \quad = \quad 3\,NiCr_2O_4 + 2\,Cr^{3+}. \qquad (8)$$

A similar reaction occurs at the opposing $NiCr_2O_4$/NiO interface where the spinel is formed by

$$2\,Cr^{3+} + 4\,NiO \quad = \quad NiCr_2O_4 + 3\,Ni^{2+}. \qquad (9)$$

Based on the ionic counter diffusion that follows from the reaction mechanism given by Eqs. (8) and (9) it is expected that the spinel formation at the Cr_2O_3/$NiCr_2O_4$ interface is about three times higher compared to that at the $NiCr_2O_4$/NiO interface [42]. Note also that the replacement of Ni by NiO can lead to local pore formation, as shown in Fig. 10h.

The increase of σ_{eff} during stage C in Figs. 4 and 5 shows an exponential behavior for the Ni containing pellets. This phenomenological observation is related to the diffusion controlled $NiCr_2O_4$ spinel formation where the increase in the length of ionic pathways correlates with the degree of spinel formation and associated grain size as illustrated in Fig. 17c. As a consequence of this increased transport length it is proposed that spinel formation exhibit a parabolic behavior [41, 64–66], which is in good agreement with the slightly sub-parabolic behavior of σ_{eff} observed in Figs. 4 and 5.

4.3.2. Electrical conductivity of Cr_2O_3 matrix

The experimental results for the evolution of σ_{eff} of Ni containing Cr_2O_3 pellets are presented in Figs. 4 and 5. In addition, Fig. 18 shows the relative increase of σ_{eff} upon exposure to air for all investigated samples. The figure illustrates that the increase is more pronounced for samples with higher Ni contents. For Ni free pellets the increase of conductivity during stage C is rather small but steady. This conductivity gain might be related to the fact that the equilibrium state of vacancies in Cr_2O_3 according to Eq. (1) was not yet reached until this stage.

4.4. Electrical conductivities at stage D during change from oxidizing to reducing atmosphere

4.4.1. Microstructure effects

During stage D, the initial decrease in σ_{eff} of the Cr_2O_3 pellets with Ni content ≥ 5 vol.% is followed by a significant increase in σ_{eff} over a short period of about 5 h. After reaching a maximum electrical conductivity at the end of stage D it follows again a slow decrease during stage E. The required time span of about 5 h to reach the maximum is identical in both batches. Note that the temporary maximum in σ_{eff} correlates with the amount of Ni, i. e. a higher amount of Ni leads to a more pronounced increase of σ_{eff} by up to two orders of magnitudes. This increase of σ_{eff} is attributed to the formation of metallic Ni due to the decomposition of $NiCr_2O_4$ under reducing atmospheres for pO_2 < 10^{-14} bar at 850 °C [27, 67]. The $NiCr_2O_4$ spinel decomposition in the applied f-gas atmosphere is given by

$$\begin{aligned} NiCr_2O_4 + H_2 \quad &= \\ V''_{Ni} + V^{\bullet\bullet}_{O} + 2\,Cr_{Cr} + 3\,O_O + Ni + H_2O. \end{aligned} \qquad (10)$$

An illustration of the possible $NiCr_2O_4$ spinel decomposition mechanisms is shown in Fig 17e. Note that NiO formation as an interim stage is unlikely since the equilibrium partial pressure for NiO at 850 °C is in the order of 10^{-13} bar, which is above the $NiCr_2O_4$ spinel decomposition pressure [67]. However, based on the available experimental data the spinel decomposition mechanism is plausible but can not be proven to be correct. It is also possible that Ni is transported by evaporation and condensation of volatile nickel-(II) hydroxide ($Ni(OH)_2$), adsorption, surface diffusion or a combination of these mechanisms [68, 69]. Independent from those mechanisms, the complete reduction of Ni could be proven by XRD analysis, as shown in Fig. 13b. The XRD pattern in Fig. 13b originates from the Cr_2O_3-20 sample removed after 12 h, re-reduction in f-gas atmosphere, i. e. after reaching the maximal σ_{eff} (cf. Fig. 9).

In summary, we propose that the observed increase of σ_{eff} during stage D is related to the release of Ni during $NiCr_2O_4$ spinel decomposition. Thereby the released Ni builds a, at least partly, percolating metallic network that promotes the transport of electrons within the Cr_2O_3 pellets as illustrated in Figs. 17f and Fig. 17g. Further evidence for Ni percolation was found for the Cr_2O_3-20 pellets during cool down. Thereby, a further increase in σ_{eff} could be observed with decreasing temperature and vice versa during re-heating. Such a behavior is typical for metallic conductors. Note also that, temperature variations in air (i, e. T var 5 and 6 at stage C) did not show an increase in σ_{eff} with decreasing temperature (cf. Table S1).

4.4.2. Electrical conductivity of Cr_2O_3 matrix

The results for the evolution of σ_{eff} during the transition from air to f-gas are shown in Figs. 8 and 9 for the

first and second batch, respectively. Note that all Cr_2O_3 pellets show an instant decrease of their σ_{eff}. This can be well explained by the extrinsic pO_2 dependency of the electrical conductivity of the Cr_2O_3 matrix as discussed in section 4.1.2. This means that lowering the pO_2 also leads to lower electrical conductivity.

4.5. Electrical conductivities at stage E during re-reduction in forming gas atmosphere

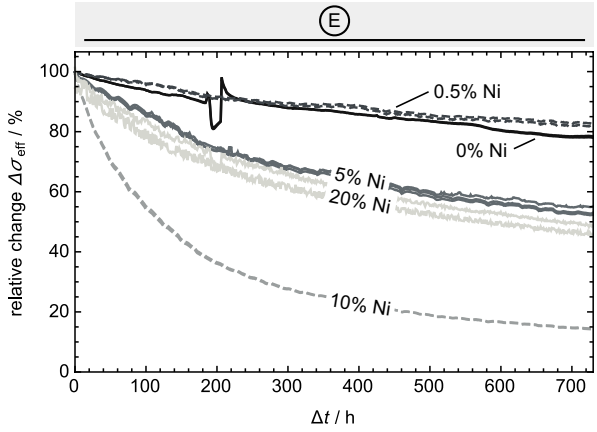

Figure 19: Relative decrease of electrical conductivities σ_{eff} of Ni containing Cr_2O_3 pellets during re-reduction in f-gas at 850 °C.

4.5.1. Microstructure effects

Superimposed on the re-equilibration of the Cr_2O_3, there is a more pronounced effect on conductivity, which largely correlates with the Ni content. It can be assumed that for the Ni containing pellets the decrease in σ_{eff} is influenced by changes in the microstructure of the metallic Ni phase. The post test analyses in Figs. 10f and 10i illustrate that Ni is more finely dispersed after oxidation and re-reduction compared to the initial particle distribution shown in Figs. 10d and 10g. Furthermore the Cr_2O_3-20 pellets removed after the spinel decomposition in stage E confirm that the metallic Ni forms a partly percolating matrix that dominates the observed σ_{eff} of the pellet. Hence the continuous decrease of σ_{eff} during stage E is probably related to the disconnection of the Ni network. The reason is that the well dispersed Ni after spinel decomposition as shown in Fig. 11a tends to minimize its surface free energy known as the Ostwald ripening [57, 70]. Thereby enlarged Ni agglomerates are formed by a condensation-evaporation mechanism [70], which decreases the connectivity of the Ni network. This process goes along with a smoothing of the edges of the Ni particles as seen in Fig. 11b compared with Fig. 11a. The mechanism of Ostwald ripening is schematically illustrated in Figs. 17g to 17h.

The corresponding relative decrease of σ_{eff} is shown in Fig. 19. Interestingly there is a clear correlation between the Ni content and the relative decrease of σ_{eff}. As expected, Cr_2O_3-0 and Cr_2O_3-0.5 pellets show similar behaviors with the lowest relative decrease followed by the Cr_2O_3-5 and Cr_2O_3-10 pellets. The Cr_2O_3-20 pellets shows a relative decrease similar to the Cr_2O_3-5 pellets. Obviously the percolating network of this Cr_2O_3-20 pellets is still intact and only sparsely effected by the Ostwald ripening, respectively.

4.5.2. Electrical conductivity of Cr_2O_3 matrix

During re-reduction in f-gas atmosphere a continuous decrease in σ_{eff} can be observed in Figs. 4, 5 and 19 for all samples. The continuous decrease of σ_{eff} for the Cr_2O_3 pellets without Ni can be explained by a successive approximation to the equilibrium state. This is confirmed by the Cr_2O_3-0 pellets, which at the end of stage E return to σ_{eff} values that are close to the initial values.

4.6. Effect of humidity on electrical conductivity

σ_{eff} is further affected by the humidification of the atmosphere. The results in Table S1 show that σ_{eff} is increased when 3–4 vol.% of water are added to f-gas and H_2 compared to the respective dry conditions. This behavior can be observed for all Cr_2O_3 pellets except for those without Ni in H_2 where humidification does not affect σ_{eff}. The mechanisms behind this behavior is not completely clear [71]. We believe that this behavior is simply related to variations of pO_2 and its influence on the conductivity of Cr_2O_3. From the measured Nernst potential it can be concluded that for dry forming gas atmosphere the oxygen partial pressure is about three orders of magnitudes lower compared to humidified atmosphere. In hydrogen the pO_2 is increased by nearly 2 orders of magnitudes when 3–4 vol.% of water are added. Based on these differences, it is likely that the Cr_2O_3 pellets feature a p-type behavior under tested conditions, where increasing oxygen pressure increases σ_{eff}. This increase of σ_{eff} can be associated to the defect structure or more precisely to the concentration of electron holes, see Eq. (1).

Note however that σ_{eff} of the Cr_2O_3-20 pellets after stage E shows a deviating behavior since the electron transport is dominated by the partly percolating Ni network. Consequently σ_{eff} is decreased with increasing temperature and vice versa. Interestingly, for samples with 20 vol.% Ni, σ_{eff} in humidified f-gas is lower than

in dry f-gas. However, with increasing temperature this difference becomes smaller. This behavior can be attributed to an increased volatility of $Ni(OH)_2$ in humidified atmospheres, which leads to agglomeration and de-percolation of Ni and associated loss of σ_{eff}. The fact that this difference of σ_{eff} becomes smaller with increasing temperature can be attributed to the semi-conductive behavior of the Cr_2O_3 matrix, which increases with temperature and hence becomes more dominant. To prove this hypothesis however further dedicated experimental work is required.

4.7. Thermal activation energy E_A

For dry f-gas, the thermal E_A was determined from the Arrhenius plot as shown in Fig. 15a. For all other conditions they are summarized in Table 3. Inspection of the thermal E_A reveals that it is reduced with increasing pO_2. In particular the thermal E_A is reduced in humidified atmospheres, since the water content increases the oxygen partial pressure. Note also that the obtained values for the thermal E_A of Cr_2O_3 in air (0.187–0.264 eV) are in good agreement with data available from the literature [54, 72].

The thermal E_A of the Cr_2O_3-20 pellets at the end of stage E is dominated by the percolating Ni network. As a consequence the determined thermal E_A become negative with values of -0.064 eV and -0.078 eV, which is characteristic for metallic conductors. The extracted E_A values in dry f-gas atmosphere are smaller compared to those determined under humidified conditions. This might also be attributed to the progressive dis-percolation of the Ni network as described in the previous section.

5. Conclusions

This study focuses on the interaction between Cr_2O_3 and Ni and on the associated variation of the electrical conductivity. These issues are related to long-term degradation phenomena, which occur on the anode side in SOFC stacks. Thereby Cr_2O_3 scales with enclosed Ni are typically formed on the metallic interconnects. Such a mixed oxide scale is shown by a representative SEM cross section image obtained after 40,000 h stack operation in Fig. 1.

Under reducing anode conditions (f-gas, stage A) the conductivity is mainly dominated by the properties of Cr_2O_3 (i. e. defect concentration and impurities). However, in samples with a Ni content of 20 vol.%, some local percolation pathways are formed within the Ni phase, which leads to elevated conductivities and a metallic behavior of conductivity upon temperature variations.

When changing to oxidizing conditions (air, stage B) there is first a fast response of the Cr_2O_3 material, which can be attributed to a thermodynamic re-equilibration including adaptations in the vacancy concentrations. This re-equilibration with the pO_2 leads to a fast and significant increase of the conductivity. In a second step, there is also a more sluggish response (stage C), which is related to spinel formation ($NiCr_2O_4$) at the expense of Ni and Cr_2O_3. The sluggish spinel formation leads to a exponential evolution of the electric conductivity. The conductivity that is finally reached upon complete transformation of Ni into $NiCr_2O_4$ spinel correlates with the total Ni content of the sample.

When changing back to reducing conditions (stages D and E), there are three main processes observed. First, a fast thermodynamic re-equilibration (with pO_2 dependent vacancy concentrations) leads to a drop in conductivity (at the beginning of stage D). Second, the decay of spinel and the associated formation of Ni is somewhat slower than the thermodynamic equilibration. It leads again to a temporary increase of the conductivity. The maximum conductivity that is temporarily reached correlates with the Ni content (end of stage D). Third, on a longer term, the newly formed Ni particles are reorganized during an extended period of up to 1000 h (stage E). The coarsening and the associated loss of percolation lead to a slow decrease in conductivity. Nevertheless, even at long reduction times (in stage E) the conductivity remains above the initial values (in stage A). This can be explained by the fact the Ni is now more finely dispersed due to a microstructure reorganization that is associated with the formation and decay of $NiCr_2O_4$ spinel.

The present investigation is considered as a basis for better interpretations of ohmic resistances occurring in SOFC stacks with metallic interconnects and with Ni containing anodes. In particular, the results indicate that at least 10 vol.% of Ni is required within the Cr-scales, in order to change the electrical properties from semi-conductive Cr_2O_3 into a metallic behavior of a (partially) percolating Ni network. Based on these findings further studies should focus on methods to increase the amount of metallic particles in thermally grown oxide scales to decrease ohmic losses at the metallic interconnect interfaces.

Acknowledgment

The authors wish to thank Swisselectric Research and the Swiss Federal Office of Energy for their financial

support within the Swiss SOF-CH ESC project. Felix Fleischhauer is thanked for sintering the investigated Cr_2O_3 pellets at EMPA Materials Science and Technology in Dübendorf, Switzerland. We also thank Tarik Oğurtani from the Middle East Technical University in Ankara, Turkey, for the useful discussion about the spinel decomposition mechanism.

A1 Supplementary data

Supplementary data to this article can be found online at http://dx.doi.org/10.1016/j.ssi.2015.11.003.

References

[1] A. Weber, E. Ivers-Tiffée, J. Power Sources 127 (2004) 273–283.
[2] V. Sauchuk, S. Megel, E. Girdauskaite, N. Trofimenko, M. Kusnezoff, A. Michaelis, Russ. J. Electrochem. 47 (2011) 522–530.
[3] K. Föger, in: Proc. 10th Eur. SOFC Forum, volume A0503, pp. A0518–A0524.
[4] A. Mai, B. Iwanschitz, R. Denzler, U. Weissen, D. Haberstock, V. Nerlich, A. Schuler, in: Proc. 10th Eur. SOFC Forum, volume A0403, pp. A0420–A0427.
[5] A. Nanjou, in: Proc. 10th Eur. SOFC Forum, volume A0202, p. A028.
[6] Q. Ma, F. Tietz, A. Leonide, E. Ivers-Tiffée, Electrochem. Commun. 12 (2010) 1326–1328.
[7] A. Buyukaksoy, V. Petrovksy, F. Dogan, ECS Trans. 45 (2012) 509–514.
[8] T. J. Armstrong, M. Smith, A. V. Virkar, ECS Meet. Abstr. #1155 (2005).
[9] S. Benhaddad, J. Protkova, W. Dueck, S. Sherman, ECS Trans. 7 (2007) 2125–2133.
[10] W. B. Guan, L. Jin, X. Ma, W. G. Wang, Fuel Cells 12 (2012) 1085–1094.
[11] W. Quadakkers, J. Piron-Abellan, V. Shemet, L. Singheiser, Mater. High. Temp. 20 (2003) 115–127.
[12] Z. Yang, Int. Mater. Rev. 53 (2008) 39–54.
[13] J. Wu, X. Liu, J. Mater. Sci. 26 (2010) 293–305.
[14] M. Linder, T. Hocker, L. Holzer, K. A. Friedrich, B. Iwanschitz, A. Mai, J. A. Schuler, J. Power Sources 243 (2013) 508–518.
[15] M. Linder, T. Hocker, L. Holzer, K. A. Friedrich, B. Iwanschitz, A. Mai, J. A. Schuler, J. Power Sources 272 (2014) 595–605.
[16] A. Mai, B. Iwanschitz, J. A. Schuler, R. Denzler, V. Nerlich, A. Schuler, ECS Trans. 57 (2013) 73–80.
[17] H. Nagai, T. Fujikawa, K.-i. Shoji, T. Jpn. I. Met. 24 (1983) 581–588.
[18] P. Huczkowski, N. Christiansen, V. Shemet, L. Niewolak, J. Piron-Abellan, L. Singheiser, W. J. Quadakkers, Fuel Cells 6 (2006) 93–99.
[19] J. Crawford, R. Vest, J. Appl. Phys. 34 (1964) 2413–2418.
[20] A. Holt, P. Kofstad, Solid State Ionics 69 (1994) 127–136.
[21] A. Holt, P. Kofstad, Solid State Ionics 69 (1994) 137–143.
[22] A. Holt, Solid State Ionics 100 (1997) 201–209.
[23] W. Zhu, S. Deevi, Mater. Sci. Eng., A 362 (2003) 228–239.
[24] A. Weber, Solid State Ionics 152-153 (2002) 543–550.
[25] J. Froitzheim, L. Niewolak, M. Brandner, L. Singheiser, W. J. Quadakkers, J. Fuel Cell Sci. Tech. 7 (2010) 031020.
[26] M. Canavar, Y. Kaplan, Int. J. Hydrog. Energ. (2014) 4–9.
[27] W. Zhu, S. Deevi, Mater. Res. Bull. 38 (2003) 957–972.
[28] K. A. Nielsen, A. R. Dinesen, L. Korcakova, L. Mikkelsen, P. V. Hendriksen, F. W. Poulsen, Fuel Cells 6 (2006) 100–106.
[29] C. Fu, K. Sun, X. Chen, N. Zhang, D. Zhou, Corros. Sci. 50 (2008) 1926–1931.
[30] L. Mikkelsen, J. Hø gh, P. Hendriksen, Proc. 8th Eur. SOFC Forum A0905 (2008) 1–10.
[31] Plansee SE, Plansee SE, 2015.
[32] T. Farrell, D. Greig, J. Phys. C 1 (1968) 1359–1369.
[33] P. Hou, J. Stringer, Mater. Sci. Eng., A 202 (1995) 1–10.
[34] A. Ul-Hamid, Oxid. Met. 58 (2002) 23–40.
[35] H. Nagai, S. Ishikawa, N. Amano, T. Jpn. I. Met. 26 (1985) 753–762.
[36] R. Hiesgen, T. Morawietz, M. Handl, M. Corasaniti, K. A. Friedrich, J. Electrochem. Soc. 161 (2014) F1214–F1223.
[37] L. Holzer, B. Iwanschitz, T. Hocker, B. Münch, M. Prestat, D. Wiedenmann, U. Vogt, P. Holtappels, J. Sfeir, A. Mai, T. Graule, J. Power Sources 196 (2011) 1279–1294.
[38] G. Archie, in: Soci. Pet. Eng., volume 146, pp. 54–62.
[39] G. Gaiselmann, M. Neumann, L. Holzer, T. Hocker, M. R. Prestat, V. Schmidt, Comp. Mater. Sci. 67 (2013) 48–62.
[40] D. Wiedenmann, L. Keller, L. Holzer, J. Stojadinović, B. Münch, L. Suarez, B. Fumey, H. Hagendorfer, R. Brönnimann, P. Modregger, M. Gorbar, U. F. Vogt, A. Züttel, F. L. Mantia, R. Wepf, B. Grobéty, AlChE J. 59 (2013) 1446–1457.
[41] C. Greskovich, J. Am. Ceram. Soc. 53 (1970) 498–502.
[42] J. S. Armijo, D. L. Douglass, R. a. Huggins, J. Electrochem. Soc. 120 (1973) 825.
[43] H. Nagai, S. Ishikawa, K.-i. Shoji, T. Jpn. I. Met. 26 (1985) 44–51.
[44] J. H. Park, K. Natesan, Oxid. Met. 33 (1990) 31–54.
[45] W. Qu, L. Jian, J. M. Hill, D. G. Ivey, J. Power Sources 153 (2006) 114–124.
[46] N. G. Eror, J. B. Wagner, Phys. Status Solidi (B) 35 (1969) 641–651.
[47] C. Osburn, R. Vest, J. Phys. Chem. Solids 32 (1971) 1343–1354.
[48] M. Pope, N. Birks, Corros. Sci. 17 (1977) 747–752.
[49] P. Kofstad, Nonstoichiometry, Diffusion and Electrical Conductivity in Binary Metal Oxides, Wiley, reprint ed edition, 1983.
[50] J. S. Park, H. G. Kim, J. Am. Ceram. Soc. 71 (1988) 173–176.
[51] H. Nagai, K. Ohbayashi, J. Am. Ceram. Soc. 72 (1989) 400–403.
[52] T. Matsui, K. Naito, J. Nucl. Mater. 120 (1984) 115–118.
[53] E. W. A. Young, P. C. M. Stiphout, J. H. W. de Wit, J. Electrochem. Soc. 132 (1985) 884.
[54] P. Kofstad, K. P. Lillerud, J. Electrochem. Soc. 127 (1980) 2410–2419.
[55] M. Linder, T. Hocker, C. Meier, L. Holzer, K. A. Friedrich, B. Iwanschitz, A. Mai, J. A. Schuler, J. Power Sources 288 (2015) 409–418.
[56] P. Kofstad, Proc. 2nd Eur. SOFC Forum, vol 2 (1996) 479–490.
[57] B. Iwanschitz, Degradation von Ni-Cermet-Anoden in keramischen Hochtemperaturbrennstoffzellen, Ph.D. thesis, Rheinisch -Westfälischen Technische Hochschule Aachen, 2012.
[58] D. Sarantaridis, A. Atkinson, Fuel Cells 7 (2007) 246–258.
[59] F. N. Rhines, J. Electrochem. Soc. 124 (1977) 1122.
[60] R. Peraldi, D. Monceau, B. Pieraggi, Oxid. Met. 58 (2002) 275–295.
[61] C. Greskovich, J. Am. Ceram. Soc. 67 (1984) 111–112.
[62] R. J. D. Tilley, Principles and Applications of Chemical Defects, CRC Press, 1st edition, 1998.
[63] J. A. Schuler, C. Gehrig, Z. Wuillemin, A. J. Schuler, J. Wochele, C. Ludwig, A. Hessler-Wyser, J. Van Herle, J. Power Sources 196 (2011) 7225–7231.
[64] H. SchmaIzried, Ber. Dtsch. Keram. Ges. 42 (1965) 11–22.
[65] H. Schmalzried, Angew. Chem. Int. Ed. 2 (1963) 251–254.

[66] F. Pettit, E. Randklev, E. Felten, J. Am. Ceram. Soc. 49 (1966) 199–203.
[67] S. C. Schaefer, Electrochemical Determination of Thermodynamic Properties of NiCr204 and CoCr204, Technical Report, US Bureau of Mines, 1986.
[68] H. Yokokawa, H. Tu, B. Iwanschitz, A. Mai, J. Power Sources 182 (2008) 400–412.
[69] B. Iwanschitz, L. Holzer, A. Mai, M. Schütze, H. Ag, Z. Park, in: Proc. 10th Eur. SOFC Forum, June, pp. A1005–A1015.
[70] J. A. Marqusee, J. Ross, J. Chem. Phys. 80 (1984) 536.
[71] Y. Larring, R. Haugsrud, T. Norby, J. Electrochem. Soc. 150 (2003) B374.
[72] R. Ku, W. Winterbottom, Thin Solid Films 127 (1985) 241–256.